Research Article Vol. 28, No. 6 / 16 March 2020 / Optics Express 8574
Optics EXPRESS

Coherent imager module with a large field of view for synthetic aperture interferometry applications

J. Garcia-Armenta, P. D. Ruiz,* J. M. Coupland, C. R. Coggrave, and R. J. C. Middleton

Wolfson School of Mechanical, Electrical and Manufacturing Engineering, Loughborough University, Epinal Way, Loughborough LE11 3TU, UK
*P.D.Ruiz@lboro.ac.uk

Abstract: Optical areal profilometry of large precision-engineered surfaces require high-resolution measurements over large fields of view. Synthetic Aperture Interferometry (SAI) offers an alternative to the conventional approach of stitching small fields of view (FOV) obtained with Coherent Scanning Interferometry (CSI) using high-NA objectives. In SAI, low-resolution digital holograms are recorded for different illumination and observation directions and they are added coherently to produce a high-resolution reconstruction over a large FOV. This paper describes the design, fabrication and characterization of a large FOV, compact and low-cost coherent imager (CI) as a building block of a coherent sensor array for a SAI system. The CI consists of a CMOS photodetector array with 1.12 µm pixel pitch, a square entrance pupil and a highly divergent reference beam that emerges from a pinhole milled with a focused ion beam on the cylindrical cladding at the tip of an optical fibre. In order to accurately reconstruct the digital holograms, the wavefront of the reference beam is estimated by localizing the reference source relative to the photodetector array. This is done using an optimization approach that simultaneously reconstructs plane waves that reach the aperture from 121 different illumination directions and guarantees a phase root-mean-squared (RMS) error of less than a fifth of the wavelength across the CI entrance pupil at a boundary of the FOV. The CI performance is demonstrated with a holographic reconstruction of a 0.110 m wide object placed at a distance of 0.085 m, i.e. a FOV = ±0.57 rad, the highest reported to date with a holographic camera.

1. Introduction

Inspection and quality control of large precision-engineered surfaces require advanced non-contact measurement solutions capable of measuring surface profile over large areas with high spatial resolution. This is usually achieved with optical profilometers based on coherence scanning interferometry (CSI), focus variation, or laser triangulation [1]. In order to measure large areas, several single measurements are stitched together, considerably increasing the data acquisition time and requiring precision stages to move the optics relative to the surface. A remarkable example of an optical metrology system for large parts is the Nanometer Accuracy Non-contact Measurement of Freeform Optical Surface (NANOMEFOS) project [2]. This high dynamic range device can measure a surface of Ø500×100 mm with a depth resolution of nanometers within minutes. However, the complex design and high-precision manufacturing required to achieve this performance for a large measurement area makes this an expensive machine for routine use in industry. A system capable of reconstructing the surface at the required resolution depending on the presence and size of defects would be able to accelerate these inspection tasks, e.g. by having the capability of locally adapting the spatial resolution in a large field.

#383912 https://doi.org/10.1364/OE.383912
Journal © 2020 Received 3 Dec 2019; revised 14 Feb 2020; accepted 15 Feb 2020; published 10 Mar 2020

Optics EXPRESS

Lens-less digital holography (DH) is an alternative approach with multiple applications including phase microscopy and surface shape and deformation measurement [3–5]. In DH, the FOV and lateral resolution are limited by the pixel pitch and photodetector array dimensions, respectively, but larger numerical apertures can be synthesized to increase both FOV and resolution by coherently adding low resolution holograms obtained for different illumination and/or observation directions. Known as synthetic aperture interferometry, this approach effectively increases the space-bandwidth product SBP (a measure of the amount of information that the optical system can capture, approximately the ratio between the area of the FOV and of the central lobe of the point spread function) [6]. SAI is a well-established technique in the fields of radar and radio astronomy, and its most extreme achievement is perhaps the first image of a black hole [7]. In optical bandwidths, SAI has been implemented with different strategies to sample frequency space, e.g. by using a single receiver while varying the object's illumination angles [8] by fixing the illumination source while moving the sensor [9], by rotating the object [10] or by having a combination of multiple sources and receivers [11].

Figure 1 illustrates different approaches to SAI. In Fig. 1(a), (a) fixed source S illuminates the surface under study, while a coherent imager CI that measures the complex field at the plane of its entrance pupil EP (by propagating the demodulated recorded holograms back to the EP) is moved laterally. The reference beam inside the CI and the illumination source both are provided by the same laser source, not shown in the figure. In Fig. 1(b) the coherent imager CI remains fixed and the source S is moved to illuminate the surface from different angles. In Fig. 1(c) an array of fixed coherent imagers CI and sources S operate sequentially so that each coherent imager measures the complex field at its entrance pupil EP for each illumination direction. Figures 1(d-f) show the Fourier domain representation of the setups shown in Fig. 1(a-c), respectively. The corresponding illumination, observation and scattering vectors $\mathbf{k}_i$, $\mathbf{k}_o$ and $\mathbf{K} = \mathbf{k_o}\text{-}\mathbf{k_i}$ are indicated, respectively. In all these cases, the three-dimensional k-space is populated with complex values measured at each spatial frequency component determined by the scattering vectors $\mathbf{K}$. A high-resolution reconstruction of the object can be finally obtained by an inverse Fourier transform of the complex field in k-space. What limits the imaging numerical aperture and therefore the angular subtense of the object from the centre of the synthetic aperture is the spatial resolution of the complex field detected at the entrance pupil of the coherent imagers, while the spatial resolution is determined by the extent of the synthetic aperture. In 3D we should more rigorously refer to a synthetic transfer function, rather than a synthetic aperture, but we will refer to synthetic aperture without loss of generality and for historical reasons. Even though the different illumination and observation configurations shown in Fig. 1 lead to a bigger synthetic aperture, it is worth noticing that they are not equivalent; they result in different transfer functions (also referred to as 'support' in k-space), which are indicated by a grey shaded region in Figs. 1(d-f). When measuring surfaces, it can be shown that the spatial frequencies in this support are directly related to those predicted in a 'foil-model' representation of the surface [12]. Other approaches to SAI in 'transmission mode' imaging include point source digital in-line holography [13], optical diffraction tomography [14] and lensless Fourier digital holography [15], usually applied to reconstruct small FOVs of a few mm^2.

The fundamental requirement in SAI is that each low-resolution hologram is recorded with a known phase relationship to all others, so that they can be combined coherently. This is normally achieved with a single reference source R placed next to the object (or at infinity), so that a spatial carrier common to all observation directions separates the interference and autocorrelation terms in the Fourier domain [16], as shown in Fig. 2. This solution, however, is not scalable and requires a reference source next to the object, which is not always feasible. An alternative approach consists of having independent coherent imagers (CI), i.e. phase-locked holographic cameras, each with its own reference source, that could be arranged in large numbers in an array as illustrated in Fig. 1(c). An optimal array would maximize the ratio between the entrance

Optics EXPRESS

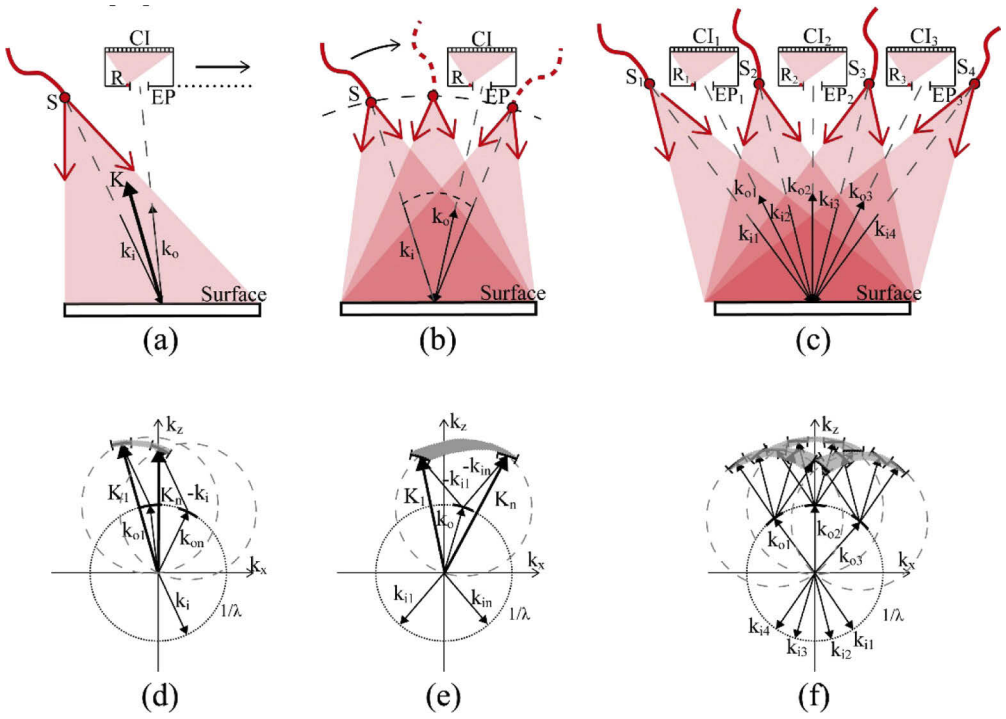

Fig. 1. Examples of different SAI configuration setups to populate frequency space. (a) Moving the coherent imager. (b) Moving the illumination source S. (c) Array of coherent imagers and array of illumination sources S. (d-f) Frequency domain representation of SAI configuration setups (a-c), respectively. The shaded regions represent the effective transfer function, whose angular subtense is known as the synthetic aperture.

pupil area to the area of the coherent sensor unit cell. The objective in SAI is therefore to coherently combine the object field at the aperture of CIs that are phase-locked and diffraction limited (according to the Rayleigh criterion, this corresponds to a phase error limited to $\lambda/4$ at the aperture).

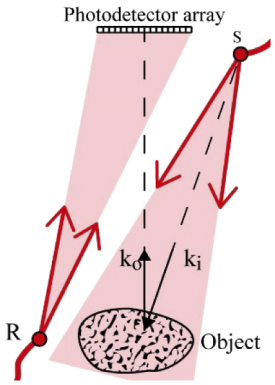

Fig. 2. Fourier off-axis hologram with spatial carrier. The distance from the sensor to the reference source and the object is much larger than the sensor dimensions (Fresnel approximation).

Optics EXPRESS

In [17], a compact CI was proposed, built by cementing a CMOS photodetector and a ferrule-terminated high-NA fibre to a 5×5×5 mm^3 beam splitter cube. A FOV ~ ±0.5 rad was achieved at 633.8 nm, using only the red pixels of a colour CMOS photodetector with 1.12 µm pixel pitch, with an entrance pupil of 0.4×0.4 mm^2. The tradeoff of having a monolithic optical unit was the presence of 3rd order Seidel distortion in the holographic reconstruction and spherical aberration in the reference beam. For CIs to be used in SAI, their reference wavefronts must be known so that the object wavefront reaching their entrance pupils can be measured without distortion and then coherently combined.

In digital holography, the reference wave is usually measured by recording a known test object wave, typically a plane wave [18] since the object beam can be well collimated by using a shearing plate interferometer, for instance [19]. The tilt of the object beam relative to the sensor, however, is difficult to measure and can be considered unknown. Spherical waves emerging from a pinhole are often used as reference waves in holographic microscopy [20]. If the position of the pinhole with respect to the photodetector is not known precisely, then both the divergence and the tilt of the test object wave at the detector are unknown. However, if the Fresnel approximation is valid (NA>>$2(ka)^{-1/2}$) being a the aperture radius [21]), it can be shown that unknown tilt and divergence of the test object wave results in a similar tilt and divergence in the estimated reference wave and has no apparent effect on image quality [22]. Reference wave tilt can also be estimated from the frequency content in the interferogram from a single off-axis digital hologram [23]. Once again, these methods are only applicable for low-NA recordings, when the Fresnel approximation is valid. In [17], a highly divergent reference beam was characterized using a digital reference wavefront to reconstruct simultaneous plane waves reaching the CI's aperture (sources at infinity). The solution to the position of the reference source is found by maximizing the power of the reconstructed sources at infinity. While a close estimate to the reference source position was found, multiple local minima in the cost function translated into an uncertainty of several microns, with an unknown effect on the phase wavefront at the plane of the entrance pupil.

In this paper, we present a diffraction limited lens-less compact digital holographic camera that can make recordings over a FOV~±0.5 rad. The new CI eliminates the beam splitter and uses all the pixels in a colour CMOS photodetector by operating it at 785 nm. This, and a larger entrance pupil, simultaneously increases the FOV and the spatial resolution as compared with the CI in [17]. Section 2 describes some design considerations; section 3 details the fabrication of the reference source, an optimal approach to characterize the reference wavefront and a discussion of the phase wavefront errors as a function of the position uncertainty of the pinhole reference source.

2. Coherent imager

The CI design presented here eliminates the cube beam splitter in [17] to avoid distortion and spherical aberrations. It incorporates a 'pinhole' reference source and an entrance pupil whose angular subtense from the photodetector limits the spatial bandwidth of the interferograms such that the Nyquist sampling criterion is achieved even at the highest spatial frequency. Figure 3 shows a schematic diagram of the CI, which is composed of a 3D printed acrylonitrile butadiene styrene (ABS) casing, a shim metal sheet with a thickness of 26 µm with a square entrance pupil EP of 1.25×1.25 mm^2, a 'pinhole' reference source and a CMOS. As discussed in detail in section 2.4, the recorded hologram is demodulated and the complex field is backpropagated from the CMOS photodetector array to the entrance pupil, where we compute a high-resolution complex field. This high-resolution field is then propagated to the object to reconstruct a large FOV but with a lower spatial resolution. The size of the EP determines the spatial resolution (i.e. the average speckle size).

Optics EXPRESS

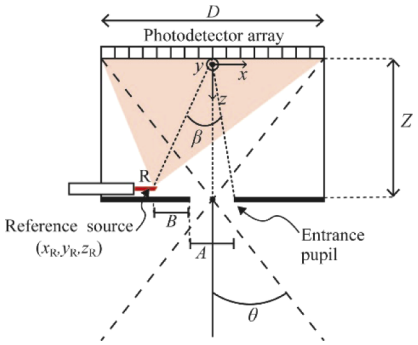

Fig. 3. Coherent imager schematic diagram.

2.1. Design considerations

The effective angular FOV $\pm\theta$ of the CI is determined from the angle subtended by the photodetector from the centre of the entrance pupil:

$$\theta = \tan^{-1}\left(\frac{D}{2Z}\right) \tag{1}$$

where D is a transverse dimension of the photodetector array and Z is the distance between the photodetector array and the plane of the entrance pupil. Equation (1) is used to establish Z given the required design FOV$\sim \pm 0.5$ rad. Dimensions A, B and Z in Fig. 3 are related to the angle β between a ray from the reference source to the centre of the photodetector array and a ray from the furthest edge of the entrance pupil to the centre of the array. β is chosen so that a hologram of the entrance pupil is band limited within the sensor resolution and to separate the cross-correlation terms in the frequency domain by a spatial carrier. One function of the aperture is to control the relationship between FOV and resolution of the object reconstruction, while another is to serve as a spatial filter so that the fringe spacing from the interference of any point in the aperture and the reference beam is larger than twice the pixel pitch, p, to prevent aliasing of the hologram, i.e.

$$2p < \frac{\lambda}{2\sin\beta} \tag{2}$$

where λ is the wavelength of the reference and illumination sources and β can be written in terms of A, B and Z as

$$\beta = \tan^{-1}\left(\frac{A/2}{Z}\right) + \tan^{-1}\left(\frac{A/2 + B}{Z}\right) \tag{3}$$

Once Z has been established from Eq. (1) for a given D and desired FOV, A can be found from Eq. (2) and (3) given p, λ and B.

2.2. Reference beam

Hahn et al proposed an interesting camera design replacing the conventional cube beam splitter with a side launch reference beam and a slab waveguide [18]. Their approach, however, leads to reference wavefront aberrations and multiple optical elements are required to couple light into a slab that guides the reference beam by total internal reflection. Here we propose a design that eliminates the beam splitter and the ferrule used in [17], and the launch optics and slab waveguide in [18]. It consists of a bare single mode (SM) fibre with its end polished at an angle of 45° to steer the beam perpendicular to the fibre core axis. The fibre is then threaded through hypodermic stainless steel tubing in order to enable effective handling for alignment of the polished face, and

Optics EXPRESS

cemented to the tubing so that the "wings" of the tubing's hub are perpendicular to the axis of the cone of light exiting the pinhole (see Fig. 4(a)). Tubing and fibre cladding are then plasma sputter coated with silver with the thickness set to prevent light leaking from the fibre except from the pinhole. It can be shown that a 60 nm silver coating would transmit less than 1% of the incident light for a wavelength λ=775 nm [24]. The grain structure of the silver coating prevents the fabrication of sub 1 µm diameter pinholes with uniform transmission and sharp edges since material removal depends on grain orientation for a given focused ion beam (FIB) current. This is solved by depositing a platinum disk on top of the silver, which is FIB milled and leads to high quality pinholes with sub µm diameters -see Fig. 4(b). This modification of the SM fibre, increases the effective NA from 0.12 to ~0.5, and allows the beam to be conveniently launched parallel to the photodetector array such that the entire sensor is illuminated. Interestingly, FIB machining can also be used to fabricate micro-lenses [25,26] and Bragg gratings on optical fibres [27]. Finally, the mounted fibre is assembled into the CI casing and a shim metal aperture is attached. This bare optical fibre with a lateral pinhole at the tip substitutes both the beam splitter and the ferrule in our previous prototype, and the launch optics and slab guide in [18] resulting in a CI that is more cost-effective, compact, and easier to assemble.

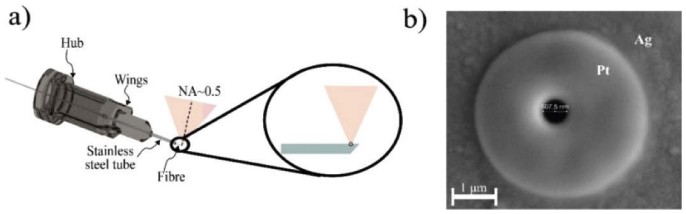

Fig. 4. (a) 45° polished fibre attached to a hypodermic tubing for handling and alignment. (b) Pinhole FIB milled onto a platinum disk deposited onto a silver coating sputtered onto the fibre cladding.

2.3. Assembly and construction of the coherent imager

A CI test rig was built on a 3D printer using PLA polymer, see Fig. 5. It incorporates the reference fibre, the aperture, and the CMOS photodetector. A Raspberry Pi single board computer is used to control the image acquisition, digitization and pre-processing of the recorded holograms. A fixed temporary FC-APC connector is used to couple the reference fibre to a SM fibre patchcord. The photodetector array is a Sony IMX219 colour photodetector commonly used in portable devices (8-bit, 3.67 × 2.76 mm^2, 3280 × 2464 pixels, pixel pitch and size p=1.12 µm, Bayer filter). The spectral response of the CMOS and Bayer filter array was measured by illuminating the photodetector with LEDs between 470 nm and 940 nm through a neutral diffuser. When illuminated with λ=785 nm, it was established that the G and B pixels are 70% and 50% as sensitive as the R ones, respectively. This means that by appropriate gain correction to the G and B pixels, the sensor can be used at its full spatial resolution. A gain correction map was calculated for all pixels by illuminating the sensor with a uniform intensity distribution of λ=785 nm, evaluating the histogram centre of mass for each filter colour and using averages of tens of images to compensate each pixel's gain so that all pixels have the same effective sensitivity. This eliminates the pattern noise and the photodetector behaves as a monochrome sensor at its highest spatial resolution when illuminated in the NIR spectrum.

Optics EXPRESS

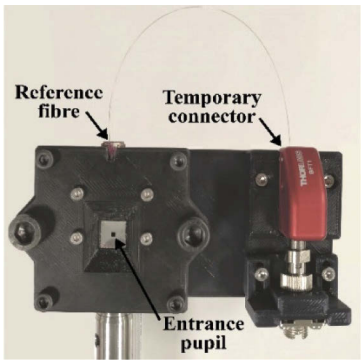

Fig. 5. Coherent imager test rig.

2.4. Hologram recording and reconstruction

In this section, we briefly discuss the methods used to calculate the complex field *at the plane of the entrance pupil*, from the intensity H of the hologram recorded at the photodetector array

$$H = |S + R|^2 = |S|^2 + |R|^2 + S^*R + SR^*, \tag{4}$$

where * represents complex conjugate. For a full mathematical description, we refer the reader to [17]. In Eq. (4), S and R are the object and reference waves, respectively. The intensity of the object and reference waves are represented by the first and second terms while the last two represent the interference or conjugate images terms. An off-axis recording geometry leads to a spatial carrier, which separates the terms in Eq. (4) in the frequency domain [28]. In the CI design presented here, the pinhole is placed close to a corner of the square entrance pupil to separate the spectra of the interference and conjugate terms, however, they will nevertheless overlap with the autocorrelation term. This is acceptable when the object wave is much weaker than the reference wave, so we can neglect the term $|S|^2$, which has the advantage of increasing the effective space bandwidth product. The recorded hologram is first demodulated by subtracting the intensity of the recorded reference wave, $|R|^2$, and by dividing the result by the complex conjugate of a numerically simulated "digital" estimate of the reference wave, R_d*, i.e.

$$U_S = \frac{H - |R|^2 - |S|^2}{R_d^*} \approx \frac{R}{R_d^*}S^* + \frac{R^*}{R_d^*}S. \tag{5}$$

The first term has a high frequency content, while the second term would be exactly S when the digital reference is equal to the true reference wave. The complex field U_S is then propagated (e.g. by using angular spectrum propagation (ASP) [28]) to the entrance pupil plane, to form the complex object wavefront U_A, where the two terms can be separated. An accurate reconstruction of the object wavefront at the entrance pupil therefore requires that the digital estimate of the reference wavefront accurately represents the amplitude and most importantly the phase of the reference wave.

2.5. Reference beam characterization

The reference beam emerging from the 0.5 µm diameter pinhole in the reference fibre can be approximated by a spherical wave

$$R(x, y) = \frac{A_0}{|\vec{r}(x, y, z)|}\exp\left[-j\frac{2\pi}{\lambda}|\vec{r}(x, y, z)|\right] \tag{6}$$

Optics EXPRESS

where A_0 is a constant and $\vec{r}$ is a vector of magnitude $|\vec{r}| = \sqrt{(x-x_R)^2 + (y-y_R)^2 + z_R^2}$ that defines the relative position of point (x, y) on the photodetector array with respect to the pinhole position (x_R, y_R, z_R), where these coordinates are relative to the central pixel in the photodetector, see Fig. 3. From Eq. (6), the reference beam can be fully characterized by establishing (x_R, y_R, z_R). The central hypothesis in our approach to determine (x_R, y_R, z_R) is that only one position of the digital reference pin-hole would lead to the correct reconstruction of plane waves reaching the entrance pupil, regardless of where they are coming from within the FOV of the CI. In other words, only one position of the estimated digital pinhole would enable the correct reconstruction of stigmatic sources at infinity, anywhere within the FOV of the CI. We call this the "Stigmatic Hypothesis". Experimentally, a set of 11×11 plane waves can be generated simultaneously by mounting a Dammann grating (DG) in front of the entrance pupil and illuminating it with a single plane wave. These plane waves pass through the entrance pupil and interfere with the spherical reference wavefront at the CMOS photodetector as seen in Fig. 6. For λ=785 nm the angle between the (0, 0) and (±5, ±5) diffraction orders is 25.9°, which corresponds to a spatial frequency $f_x = \sin(\theta)/\lambda = 5.55 \times 10^5 \mathrm{m}^{-1}$ or 1.8 µm/cycle.

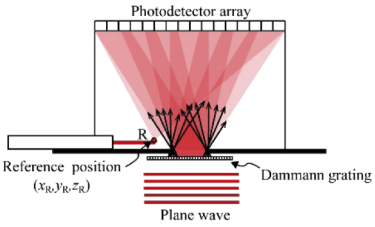

Fig. 6. Experimental setup for reference wavefront characterization.

The characterization process involves the following steps:

1) Record the intensity of the reference beam alone, $|R|^2$;
2) Record the intensity of the Object beam alone, $|S|^2$ (DG diffraction orders);
3) Record the interference between the DG diffraction orders and the reference beam, H;
4) Remove the effect of the Bayer filter to $|R|^2$, $|S|^2$, and H using calibration data for the NIR illumination wavelength used (i.e. flat field correction);
5) Establish an initial guess of the digital reference beam pinhole position, (x_{R0}, y_{R0}, z_{R0}) according to the imager casing design. This was defined by setting x_{R0} and y_{R0} equal to the designed EP corner position where the reference beam pinhole should be closely located, while z_{R0} was set as the designed stand-off distance between the CMOS sensor and the entrance pupil;
6) Set the amplitude of the estimate reference wave as the square root of the measured reference intensity image, i.e. $|A_0/|\vec{r}||^2 = \sqrt{|R|^2} \Big/ \sqrt{(x-x_{R0})^2 + (y-y_{R0})^2 + z_{R0}^2}$ and calculate the complex reference field in the plane of the photodetector according to Eq. (6) using the initial guess (x_{R0}, y_{R0}, z_{R0});
7) Subtract the terms $|R|^2$ and $|S|^2$ from H.

   As discussed in section 2.4, if the reference field is much brighter than the aperture field, then the $|S|^2$ term can be neglected and step (2) can be omitted;

Optics EXPRESS

8) Oversample the intensity field $H - |R|^2 - |S|^2$ (e.g. by zero padding its Fourier spectrum) to support the spectrum of the demodulated hologram (which will be evaluated in step (9)), where the term R/R_d^* introduces high spatial frequencies;

9) Divide the oversampled version of $H - |R|^2 - |S|^2$ by the complex conjugate of the digital reference field R_d^*. A first estimate of the complex field at the photodetector, U_{s0}, is thus obtained, according to Eq. (5);

10) Propagate (using ASP) the demodulated field U_{s0} from the photodetector plane to the entrance pupil using a distance z_{EP} chosen to provide a best focus image of the aperture. This results in the first estimate of the complex field U_{A0} at the entrance pupil plane;

11 The field at the entrance pupil, U_{A0}, is multiplied by a numerical mask that zeroes all points that fall outside the reconstructed aperture to filter out a conjugate term and the defocused reference source close to one corner of the aperture. In this case, the mask is the product of horizontal and vertical Hanning windows across the square aperture, to reduce the contribution of points around the edge. Finally, a 2D Fourier transform is applied to this masked field to reconstruct the diffraction orders of the DG at infinity (11×11 orders in a square grid).

12 A cost function Q is evaluated as an indicator of the quality of the hologram reconstruction. It is defined as [17]:

$$\mathrm{Q} = \sum_{m=-5}^{5} \sum_{n=-5}^{5} \frac{1}{I_{m,n}} \tag{7}$$

where *m, n* are indices indicating the diffraction order of the Dammann grating, M is the total number of diffraction orders (121 in this case) and $I_{m,n}$ is the peak intensity of diffracted order (m, n). If the digital reference pinhole position (x_{R0}, y_{R0}, z_{R0}) is equal to the true position (x_R, y_R, z_R), then we would obtain an accurate object reconstruction, i.e. diffraction limited stigmatic sources corresponding to the DG diffraction orders. In this case the peak intensity at each order would be maximum and $Q(x_R, y_R, z_R)$ would be minimum. Otherwise, the diffraction orders will suffer from a combination of tilt and defocus depending on the position of the diffraction order in the FOV and on the offset between (x_{R0}, y_{R0}, z_{R0}) and the true pin-hole position (x_R, y_R, z_R). The peak intensity of these aberrated diffraction orders would be reduced and Q would consequently show a higher value. It is worth noting that other cost functions can be used (e.g. the sum of the order's Strehl ratio, tranverse standard deviation of their 2D Gaussian fit, power within the first diffraction lobe, etc), but they all incur a higher computational cost. Q as defined in Eq. (7) can be interpreted as a minimum entropy approach in the information science sense, as it corresponds to a state where all the energy is concentrated tightly in the diffraction orders.

In Park et al [17], steps (1)-(12) were repeated in an iterative process to find the digital reference pin-hole position that minimizes the cost function Q. However, it was later observed that Q had multiple local minima which will trap the minimization approach (gradient descent) and the solution would depend on the initial guess (x_{R0}, y_{R0}, z_{R0}). Zernike polynomials were added as an error term to the reference wavefront on the photodetector plane to account for aberrations of the DG diffraction orders, which helped also to partially compensate for spherical aberration due to the glass beam splitter cube used and for the uncertainty in the pinhole localization. This uncertainty could reach to several tens of micrometers.

In this work, by numerically modelling hologram formation and the object field reconstruction we could establish that the reason for the local minima in [13] was the discretization of the Fourier space in step (11), in which the DG orders are reconstructed. By increasing the resolution (>10 pixels across central peak for each diffraction order) and by fitting a 4^{th} order polynomial to it, a better estimate of peak maximum power was obtained, which reduced the oscillations in the cost

Optics EXPRESS

function by a factor of 20, thus eliminating thousands of local minima. To gain some insight on the cost function "landscape", we followed steps (1)-(12) and moved the digital reference pinhole with 10 µm steps in x, y and z directions within a region of $110 \times 110 \times 110$ µm^3 around an initial guess that corresponds to the centre of the volume. Figure 7(a) shows the cost function within this volume. The slices intersect at a minimum found through cubic spline interpolation. Next, we explored the cost function around this minimum at a finer resolution by moving the estimate reference pinhole with 0.25 µm steps within a region of $4.25 \times 4.25 \times 4.25$ µm^3. Figure 7(b) shows the cost function within this volume and reveals a periodic structure that contains some local minima around a global minimum located where the slices intersect.

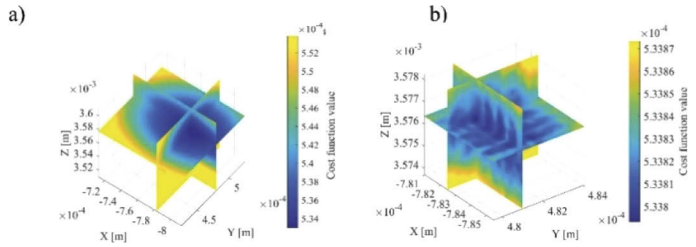

Fig. 7. 3D cost function Q within: (a) a $110 \times 110 \times 110$ mm^3 volume around an initial guess (that corresponds to the centre of the volume); (b) a $4.25 \times 4.25 \times 4.25$ µm^3 volume around the minimum found in (a) via interpolation.

Figure 8(a)-(c) shows the cost function in Fig. 7(b) along lines parallel to the x, y and z axis, respectively, that intersect at the global minimum found at x_R= - 782.437 µm, y_R = 481.014 µm and z_R = 3576.346 µm, which corresponds to the pinhole position that best satisfies the 'stigmatic hypothesis'. It can be seen that defocus (shift along z) causes bigger changes of the cost function than tilt (shift along x or y), while tilt is responsible for the periodic pattern due to the effect explained above. Figure 9 shows, in reverse contrast, the DG diffraction orders obtained from step (12) by using this optimum pinhole position. A low amplitude speckle field can be seen in the background, as expected in an experimental reconstruction.

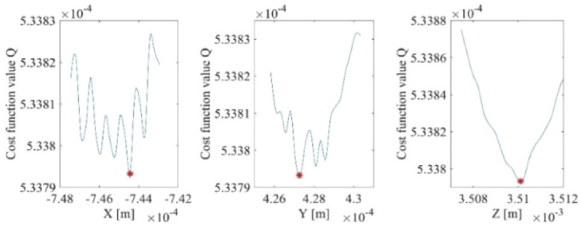

Fig. 8. Cost function along lines parallel to the x, y and z axes, that pass through the global minimum.

2.6. Phase errors

In this section, we consider each DG diffraction order independently (i.e. masking out all others) and evaluate its corresponding RMS unwrapped phase deviation from an ideal plane wavefront. While the Rayleigh criterion limits the peak-to-valley phase error to $\lambda/4$, this is for cases in which the wavefront error varies smoothly within the aperture (e.g. a spherical vs a parabolic wavefront) and all aperture points contribute equally to the point-spread-function. In our case, the phase error has localized higher values close to the edges of the aperture. Moreover, in step 11 in Section 2.5, we used Hanning windows to reduce the contribution of the phasors close to the

Optics EXPRESS

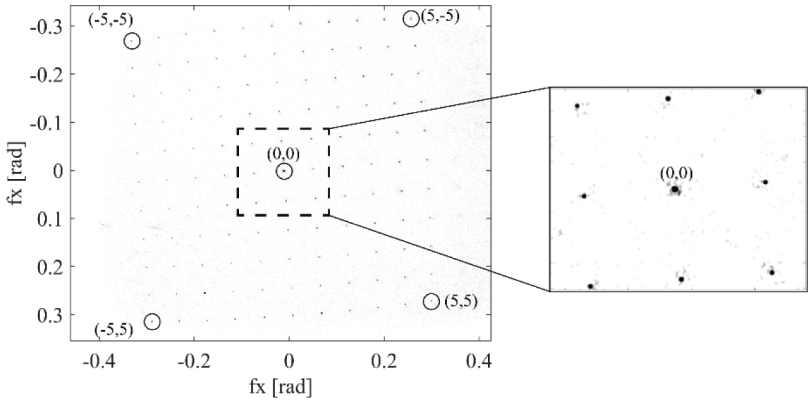

Fig. 9. Reverse contrast image of the holographic reconstruction of the Dammann grating diffraction orders at infinity using the pinhole position that satisfies the 'Stigmatic Hypothesis'.

aperture edges. For these reasons, we evaluate the phase error across the full aperture using the RMS and report relevant values of the peak-to-valley error for best and worst cases. The complex field of each diffraction order is back propagated from infinity to the entrance pupil plane using an inverse Fourier transform (effectively undoing step (11) for that diffraction order). In the ideal case, the wavefront obtained would be a tilted plane. Reconstruction quality can therefore be characterized by computing the unwrapped phase deviation (RMS or peak-to-valley) from the best-fit plane wavefront, which will increase as the mismatch between the estimated reference beam pinhole position (x_{R0}, y_{R0}, z_{R0}) and the true position (x_R, y_R, z_R) increases. Analysis for diffraction orders (0,0) and (-5,5), corresponding to the central and largest order within the field of view (see Fig. 9) are discussed below.

Figure 10 shows the RMS unwrapped phase error for a range of offsets of the estimated reference beam pinhole from the global minimum, expressed in units of wavelengths for λ=785 nm.

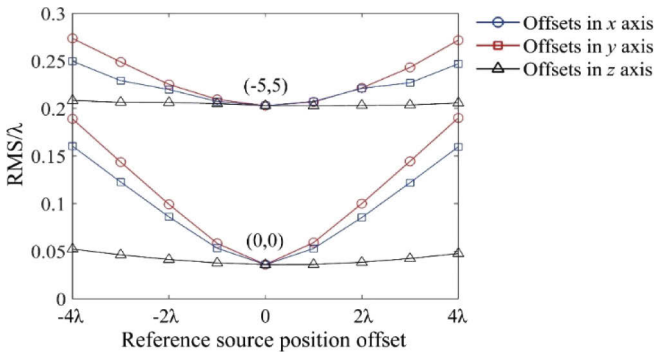

Fig. 10. RMS wavefront error from plane of best fit for the (0, 0) (bottom plots) and the (-5, 5) (top plots) DG diffraction order as the digital reference pinhole position offset varies along the x, y and z directions. Note that the separation between local minima in Figs. 7 and 8 correspond to 0.73μm, or 0.93 λ.

It indicates that a pinhole localization uncertainty of $\pm 4\lambda = \pm 3.14$μm leads to a wavefront distortion from an ideal plane wave with an RMS error below $\lambda/3$ in the worst case for oblique incidence from order (-5, 5) and below $\lambda/5$ for nearly normal illumination that corresponds to order (0, 0). At the global minimum, this error is less than $\lambda/25$ for the (0, 0) order. The non-zero

Optics EXPRESS

RMS wavefront error at zero offset in Fig. 10 for both (0, 0) and (-5, 5) diffraction orders is due to a combination of speckle noise and a residual wavefront curvature at the aperture.

In terms of the peak-to-valley error, it was established that for more than 90% of the aperture area it falls within a range of $\sim\lambda/10$ for orders (0, 0), (-5,-5) and (5,5); The worst case among all 121 diffraction orders is order (-5, 5), for which more than 90% of the aperture area has an error within a range of $\sim\lambda/2$. This is encouraging in the context of SAI as it means that the coherent imager is close to diffraction limited performance across most of the FOV.

3. Holographic reconstruction of a large field of view

An optical setup based on the configuration shown in Fig. 1(a) was used. A fibre pigtailed NIR laser (Thorlabs LP785-SAV50, FBG frequency stabilized, coherence length >>1 m, λ=785 nm, power 10 mW) was split into two arms: one to provide the reference wave inside the CI, the other to illuminate the object. The reference beam pinhole position was estimated using a Dammann grating based on the procedure described in section 2. Holograms of different objects were recorded with the coherent imager and were reconstructed following steps (1)-(11) in Section 2.5 above. Figure 11(a) shows an aluminium part ~110 mm wide placed ~85 mm in front of the entrance pupil. For this case, the FT in step (11) in Section 2.5 included a quadratic phase term to focus the plate in the final reconstruction. This corresponds to the Fresnel approximation as the angular subtense of the 1.25 mm aperture from the centre of the plate corresponds to a small NA = 7.35×10^{-3}. Figure 11(b) shows a close-up of a nickel on polymer micro mesh with a wire width ~50 µm that was placed at ~1 mm in front of the entrance pupil, observed in 'transmission mode'. For this case, the FT in step (11) in Section 2.5 was replaced by a reconstruction of the object using angular spectrum propagation. Figures 11(c) and (d) show their respective digital holographic reconstructions, with an effective FOV = ±0.57 rad, which is consistent with a reconstructed EP up sampled from 1.12 mm to 0.72 µm in step (8) in Section 2.5 to accommodate the high frequencies of the term R/R_d^* during hologram demodulation.

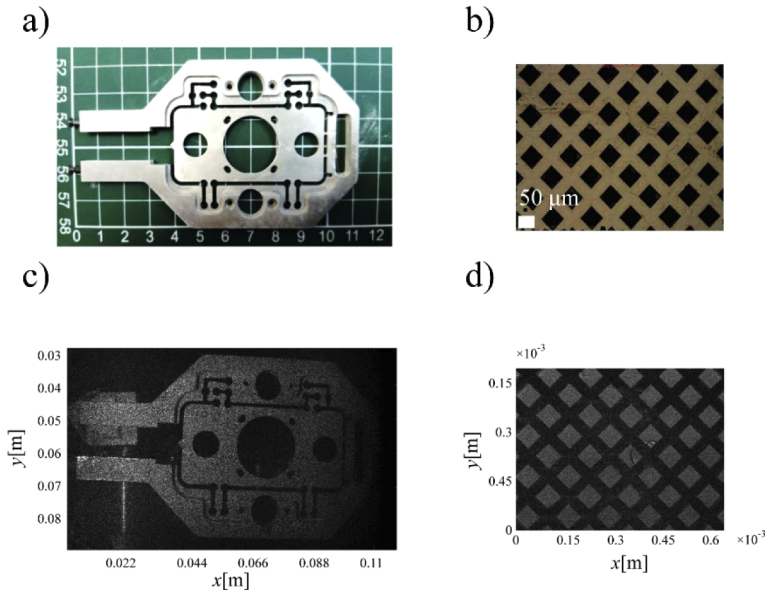

Fig. 11. (a) Machined aluminium component (grid 1 cm/div); (b) Nickel-on-polymer micro mesh with pitch ~50 µm; (c) & (d) holographic reconstruction of objects (a) and (b) placed at ~85 mm and ~1 mm in front of the CI entrance pupil, respectively.

Optics EXPRESS

According to the Rayleigh criterion for a square aperture, the spatial resolution obtained for the reconstruction of the plate and the micro mesh is 53 µm and 0.63 µm, respectively.

4. Conclusions

We presented a lensless, diffraction limited holographic camera that incorporates a highly divergent reference beam launched close to the photodetector array. The reference source is a pinhole FIB milled on the cladding at the tip of a fibre which was polished at 45 degrees to steer the beam perpendicular to the fibre axis. A 0.5 µm diameter pinhole leads to a high-NA reference beam that can reach all pixels on the photodetector array. This enables a compact digital holographic camera setup without occluding the FOV with the reference fibre. The required aperture size and distance to the photodetector array were calculated to achieve the desired FOV for the given sensor size, pixel pitch, and wavelength. The resulting FOV ~ ±0.57 rad is to our knowledge the largest reported for a lens-less coherent imager. The reference pinhole is located near one of the corners of the square aperture such that the interference and conjugate terms do not overlap. Overlap with the autocorrelation term is acceptable when the reference beam is much brighter than the object beam and has the advantage of increasing space-bandwidth product by a factor of 4 (compared to a configuration that avoids overlap with the autocorrelation term). Due to the high divergence of the reference beam, the Fresnel approximation is not valid and therefore the usual off-axis hologram demodulation method which consists of filtering its Fourier transform to remove the spatial carrier cannot be applied. Instead, we model the reference beam as a spherical wave which is fully characterized by the position of the pinhole with respect to the photodetector array. The pinhole position is found through an optimization approach based on the hypothesis: when the aperture is illuminated by a family of plane waves, there can exist only one pinhole position that would produce (via hologram demodulation and object reconstruction) stigmatic sources at infinity, regardless of their position in the FOV. It is shown that the presence of local minima in the cost function could lead to incorrect solutions for iterative approaches such as steepest descent or conjugate gradient, leading to phase errors at the entrance pupil plane unless care is taken with numerical sampling rates. Analysis of phase errors in reconstructed Dammann grating diffraction orders is presented based on the reference beam pinhole position corresponding to the global minimum. This unwrapped phase error evaluated for plane waves and expressed as a RMS deviation from a plane of best fit, is shown to be less than $\lambda/25$ at the global minimum and less than $\lambda/5$ when the pinhole position error is offset by up to 4λ. The origin of the residual wavefront curvature error at the aperture is unknown, but it may be attributed to a non-spherical reference wavefront. Multiple scattering at the walls of an imperfect pinhole, surface plasmon resonances in the metallic coating and polarization effects could lead to a non-spherical reference wavefront even for pinhole diameters smaller than λ. These effects would perturbate the wavefront more at the edges than at the centre, which may explain why the (-5, 5) diffraction order has a larger RMS wavefront error in Fig. 10.

In practical SAI systems, there is a redundancy of information as many measurements with different combinations of illumination direction, observation direction and wavelength can contribute to the same spatial frequency, as shown in Fig. 1 in the shaded areas that represent the synthetic transfer function for different configurations. A perfect, diffraction limited, coherent imager would not 'spread' phase/amplitude errors and therefore will not compromise the reconstructed object function spatial frequencies. While our coherent imager has diffraction limited performance in most of the FOV, it introduces some aberrations at the edges. These are due to phase errors close to the edge of the CI's aperture which can be measured and compensated to a certain degree to obtain diffraction limited performance. If unchecked, the effect would be that the synthetic transfer function would have phase errors that will 'spread' and add up in k-space. The phase error RMS reported above would be directly related to the quality of the

Optics EXPRESS

object function reconstruction, mainly affecting the spatial frequencies close to the 'surface' of the synthetic transfer function, as the phase errors are higher around the edges of the CI's aperture.

Funding

Engineering and Physical Sciences Research Council (EP/M020940/1); Department for Business, Energy and Industrial Strategy; UK's National Measurement System Programmes.

Disclosures

The authors declare no conflicts of interest.

References

1. R. Leach, *Optical measurement of surface topography*, (Springer, 2011).
2. R. Henselmans, G. P. H. Gubbels, C. van Venrooy, and J. A. P. Leijtens, "NANOMEFOS non-contact measurement machine for aspheric and freeform optics," Proc. SPIE **35**(4), 607–624 (2011).
3. U. Schnars and W. P. O. Jüptner, "Digital recording and numerical reconstruction of holograms," Meas. Sci. Technol. **13**(9), R85–R101 (2002).
4. P. Marquet, B. Rappaz, P. J. Magistretti, E. Cuche, Y. Emery, T. Colomb, and C. Depeursinge, "Digital holographic microscopy: a noninvasive contrast imaging technique allowing quantitative visualization of living cells with subwavelength axial accuracy," Opt. Lett. **30**(5), 468–470 (2005).
5. C. G. Tavera-R, M. H. De la Torre, J. M. Flores, M. Del Socorro, F. Mendoza, M. Briones, and J. Sanchez, "Surface structural damage study in cortical bone due to medical drilling," Appl. Opt. **56**(13), F179–F188 (2017).
6. T. M. Turpin, L. H. Gesell, J. Lapides, and C. H. Price, "Theory of the synthetic aperture microscopy," Proc. SPIE **2566**, 230–240 (1995).
7. Event horizon telescope collaboration, "First M87 event horizon telescope results. IV. Imaging the central supermassive black hole," ApJ **875**(1), 52 (2019).
8. P. Feng, X. Wen, and R. Lu, "Long-working-distance synthetic aperture Fresnel off-axis digital holography," Opt. Express **17**(7), 5473–5480 (2009).
9. F. Le Clerc and M. Gross, "Synthetic-aperture experiment in the visible with on-axis digital heterodyne holography," Opt. Lett. **26**(20), 1550–1552 (2001).
10. R. Binet, J. Colineau, and J.-C. Lehureau, "Short-range synthetic aperture imaging at 633 nm by digital holography," Appl. Opt. **41**(23), 4775–4782 (2002).
11. S. T. Thurman and A. Bratcher, "Multiplexed synthetic-aperture digital holography," Appl. Opt. **54**(3), 559–568 (2015).
12. J. Coupland, R. Mandal, K. Palodhi, and R. Leach, "Coherence scanning interferometry: linear theory of surface measurement," Appl. Opt. **52**(16), 3662–3670 (2013).
13. W. Luo, A. Greenbaum, Y. Zhang, and A. Ozcan, "Synthetic aperture-based on-chip microscopy," Light: Sci. Appl. **4**(3), e261 (2015).
14. V. Lauer, "New approach to optical diffraction tomography yielding a vector equation of diffraction tomography and a novel tomographic microscope," J. Microsc. **205**(2), 165–176 (2002).
15. L. Granero, V. Micó, Z. Zalevsky, and J. García, "Synthetic aperture superresolved microscopy in digital lensless Fourier holography by time and angular multiplexing of the object information," Appl. Opt. **49**(5), 845–857 (2010).
16. W. M. Brown and L. J. Leonards, "An introduction to synthetic-aperture radar," IEEE Spectrum **6**(9), 52–62 (1969).
17. I. S. Park, R. J. C. Middleton, C. R. Coggrave, P. D. Ruiz, and J. M. Coupland, "Characterization of the reference wave in a compact digital holographic camera," Appl. Opt. **57**(1), A235–A241 (2018).
18. J. Hahn, D. L. Marks, K. Choi, S. Lim, and D. J. Brady, "Thin holographic camera with integrated reference distribution," Appl. Opt. **50**(24), 4848–4854 (2011).
19. D. Malacara, *Optical Shop Testing*, Wiley series in Pure and Applied optics (Wiley, 2007).
20. E. Cuche, P. Marquet, and C. Depeursinge, "Simultaneous amplitude-contrast and quantitative phase-contrast microscopy by numerical reconstruction of Fresnel off-axis holograms," Appl. Opt. **38**(34), 6994–7001 (1999).
21. C. J. R. Sheppard, P. P. Roberts, and M. Gu, "Fresnel approximation for off-axis illumination of a circular aperture," J. Opt. Soc. Am. **10**(5), 984–986 (1993).
22. T. R. Hillmann, T. Gutzler, S. A. Alexandrov, and D. D. Sampson, "High-resolution, wide-field object reconstruction-with synthetic aperture Fourier holographic optical microscopy," Opt. Express **17**(10), 7873–7892 (2009).
23. P. Qiu, Z. Mei, and T. Pang, "Extracting the parameters of digital reference wave from a single off-axis digital hologram," J. Mod. Opt. **62**(10), 816–821 (2015).
24. E. D. Palik ed., *Handbook of optical constants of solids* vol. I, (Academic, 1985).
25. H. Melkonyan, K. Al Qubaisi, A. Khilo, and M. Dahlem, "Optical fibre lens with parabolic effective index profile fabricated using focused ion beam," in *Conference on Lasers and Electro-Optics, OSA Technical Digest (2016)* (Optical Society of America, 2016), paper SM1P.3.

Optics EXPRESS

26. S. Cabrini, C. Liberale, D. Cojoc, A. Carpentiero, M. Prasciolu, S. Mora, V. Degiorgio, F. De Angelis, and E. Di Fabrizio, "Axicon lens on optical fiber forming optical tweezers, made by focused ion beam milling," Microelectron. Eng. **83**(4-9), 804–807 (2006).
27. J. Huang, A. Alqahtani, J. Viegas, and M. S. Dahlem, "Fabrication of optical fibre gratings through focused ion beam techniques for sensing applications," in *Processdings of Photonics Global Conference* (IEEE 2012), pp. 1–4.
28. J. Goodman, *Introduction to Fourier Optics*, (McGraw Hill, 1966).